A solution method for the sub-surface stresses and local deflection of a semi-infinite inhomogeneous elastic medium

Article *in* Applied Mathematical Modelling · August 2012

DOI: 10.1016/j.apm.2011.10.006

CITATIONS
4

READS
59

3 authors:

S. J. Chidlow
Liverpool John Moores University
15 PUBLICATIONS **44** CITATIONS
SEE PROFILE

M. Teodorescu
University of California, Santa Cruz
57 PUBLICATIONS **464** CITATIONS
SEE PROFILE

Nicholas D. Vaughan
Cranfield University
73 PUBLICATIONS **758** CITATIONS
SEE PROFILE

A solution method for the sub-surface stresses and local deflection of a semi-infinite inhomogeneous elastic medium

S. J. Chidlow[1], M. Teodorescu[1 1,2], N.D. Vaughan[1]

[1]*Department of Automotive Engineering, School of Engineering, Cranfield University, Cranfield, MK43 0AL, UK*
[2] *Baskin School of Engineering, University of California at Santa Cruz, CA USA*

Abstract

This paper proposes analytical Fourier series solutions (based on the Airy stress function) for the local deflection and subsurface stress field of a two-dimensional graded elastic solid loaded by a pre-determined pressure distribution. We present a selection of numerical results for a simple sinusoidal pressure which indicates how the inhomogeneity of the solid affects its behaviour. The model is then adapted and used to derive an iterative algorithm which may be used to solve for the contact half width and pressure induced from contact with a rigid punch. Finally, the contact of a rigid cylindrical stamp is studied and our results compared to those predicted by Hertzian theory. It is found that solids with a slowly varying elastic modulus produce results in good agreement with those of Hertz whilst more quickly varying elastic moduli which correspond to solids that become stiffer below the surface give rise to larger maximum pressures and stresses whilst the contact pressure is found to act over a smaller area.

Keywords: Contact mechanics, Graded elasticity, Functionally graded materials

1. Introduction

The mechanical properties of a coating are often far from homogeneous. This may be intentional or could occur as a side effect of the manufacturing technique. Additionally, transition zones whose nature is dependent on the coating technology used may emerge at the interface between the coating and substrate. Consequently, it is of vital importance to determine the likely effects of using a particular coating in advance through a combination of experimental testing and mathematical modelling.

One of the earliest attempts made at determining the stress field within an elastic solid was by Boussinesq [1] who established analytic expressions for the stresses within a three-dimensional homogeneously elastic solid. This solution was adapted by Flamant [2] to predict the stress field and deformation due to a point force. However, these solutions do not consider protective layers or take account of inhomogeneities in material properties. The first generation of models to take account of a protective layer were either applicable for the idealised conditions of a thin layer (Hannah

[1]*Corresponding author's email address : mteodorescu@soe.ucsc.edu*

[3], Bentall and Johnson [4]) or a thicker layer with elastic or viscoelastic behaviour (Johnson [5], O'Sullivan and King [6], Jaffar [7], Barber [8]). Although computationally efficient, these models assume that the protective coating is homogeneous and are restricted to specific contact geometries which limits their applicability in many practical problems.

A separate class of surface treatments can achieve better load carrying capacity by gradually changing material properties with depth. There are several traditional techniques such as heat treatment or vapour decomposition which ensure a gradual transition from the properties of the outermost layer to the ones of the base material. Although these are probably the oldest surface treatments, predictive models for these processes were not attempted until recently. This was partly due to the mathematical complexity required for such models and partly due to a lack of ability to manufacture surfaces with a precisely controlled modulus of elasticity. The earliest closed-form solutions to problems of this kind were given by Gibson [9] and Booker [10]. However, these investigations were somewhat limited as Gibson considered only deep inhomogeneously elastic media whilst Booker produced a solution valid for only one particular value of Poisson's ratio. Recent advances in fabrication techniques have provided unprecedented control over the chemical structure and grain size. Consequently, deposition of elastic and viscoelastic nano-scale multi-layers have become essential for low friction and wear resistant coatings. Suresh *et al.* [11] [12] proved that functionally graded materials (FGM) can improve surface resistance to the frictional sliding contact. However, finding the optimal gradient requires accurate modelling.

A common approach is to assume that both elastic media (layer and substrate) are homogeneous in the vicinity of the computational grid point. Therefore, the approach initially proposed by Sneddon [15], which considers the wave-like nature of the localised deformation can be applied. The influence of each individual Fourier harmonic is computed and the overall solution is predicted using Bernoulli's superposition principle. This general approach proved accurate for homogeneous layers (e.g. Polansky and Keer [16], Liu and Wang [17], Tripp *et al.* [18] and Teodorescu *et al.* [19]). Xu and Zhou [20] also use this approach in their consideration of an FGM plate of continuously varying thickness which is simply supported at its four edges as they use a Fourier series expansion in both horizontal coordinates to derive a solution. Another approach that has been used successfully to compute the pressure and stress fields in an FGM material is to use Fourier transform techniques. Guler and Erdogan [13] considered a solid comprising an FGM layer with an exponentially varying shear modulus bonded to an infinitely deep homogeneous substrate. The surface of this solid was then indented by a sliding rigid punch. The problem was formulated in terms of the displacement components and the main goal was to study the initiation of fracture. Ke and Wang [14] consider the same problem as Guler and Erdogan except that they consider representing the shear modulus as a piecewise linear function over several layers instead of an exponential function. Their results are in good agreement with Guler and Erdogan but their solution is perhaps more useful as it can be used to simulate a wider range of shear moduli. The work of Giannakopoulos and Suresh [22] considers allowing the Young's modulus of the material under study to vary both linearly and exponentially with the depth coordinate. They consider applying a pressure to the surface of the material in the form of a point force and give analytic solutions

to these problems which are compared with numerical approximations produced using the finite element method.

In this work, we attempt to model the sub-surface stress field induced within an infinitely deep inhomogeneously elastic solid under pressure. It is assumed that if the contact footprint is small relative to the horizontal dimensions of the solid, only a small part of the solid in close proximity to the contact area is affected by the pressure force. The layout of this paper is as follows. In section 2, we introduce the mathematical problem and show how it may be solved and in section 3 produce numerical results for a simple symmetrical pressure. In section 4, we show how the derived expression for the vertical displacement may be used to formulate an algorithm to solve for the contact half-width and pressure force which results from a punch problem and present a selection of results for a cylindrical stamp that allows us to compare our results with those of Hertz. Our conclusions are presented in section 5.

2. Method of solution

We consider a semi-infinite, inhomogeneous, linearly-elastic solid in a state of plane strain. The solid is deemed to be locally isotropic and has a constant Poisson's ratio ν.We adopt a cartesian coordinate formulation in the (x,y) plane with the y-axis directed positively upwards and let Young's modulus be a function of the vertical coordinate. Specifically, we let

$$E(y) = E_0 e^{\alpha y}, \tag{1}$$

where E_0 is a constant which represents the value of Young's modulus on the surface of the solid and α is a constant which may be positive or negative. Figure 1 shows a logarithmic plot of Young's modulus for several arbitrary values of $\hat{\alpha} = \alpha a$, where a represents the half-contact width.

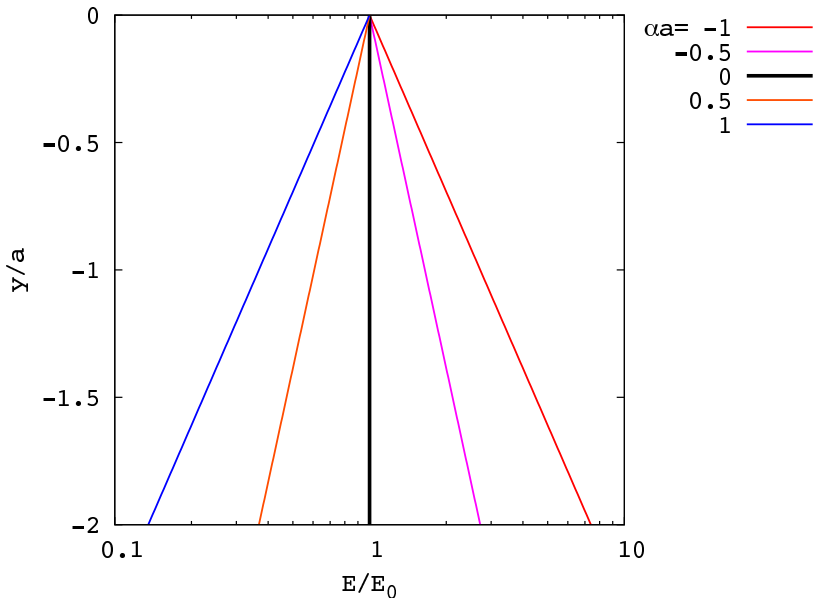

Figure 1: Examples of Young's modulus for selected values of $\hat{\alpha}$

In order to model this problem, we use the compatibility condition valid for a two-dimensional problem in the absence of gravitational body forces to derive a partial differential equation (PDE) from which we can determine the relevant Airy stress function. Following Sadd [21], we find that the stress function must satisfy:

$$\nabla^4\phi - 2\alpha\frac{\partial}{\partial y}\left(\nabla^2\phi\right) + \alpha^2\nabla^2\phi - \frac{\alpha^2}{1-\nu}\frac{\partial^2\phi}{\partial x^2} = 0 \tag{2}$$

where

$$\nabla^2 = \frac{\partial^2}{\partial x^2} + \frac{\partial^2}{\partial y^2}$$

is the Laplacian operator. It should be noted that if $\alpha = 0$, equation (2) reduces to the biharmonic equation which is to be expected as this value corresponds to a homogeneous material. The stress function ϕ is related to the components of stress within the solid via

$$\sigma_{yy} = \frac{\partial^2\phi}{\partial x^2}, \qquad \sigma_{xx} = \frac{\partial^2\phi}{\partial y^2}, \qquad \tau_{xy} = -\frac{\partial^2\phi}{\partial x\partial y}. \tag{3}$$

The horizontal and vertical displacements within the solid are related to the stress function via

$$\frac{\partial u}{\partial x} = \frac{(1+\nu)}{E(y)}\left((1-\nu)\frac{\partial^2\phi}{\partial y^2} - \nu\frac{\partial^2\phi}{\partial x^2}\right), \tag{4}$$

$$\frac{\partial v}{\partial y} = \frac{(1+\nu)}{E(y)}\left((1-\nu)\frac{\partial^2\phi}{\partial x^2} - \nu\frac{\partial^2\phi}{\partial y^2}\right). \tag{5}$$

The idea in this paper is to solve the contact problem on a finite width interval. In order for this idea to be utilised effectively, the width of the interval must be chosen to encapsulate the salient features of the problem whilst at the same time being sufficiently small to keep computational expense to a minimum.

Let the solid under study occupy the semi-infinite region $-\infty < y \leq 0, -L \leq x \leq L$ so that (2) must be solved on this domain. It is now left to determine appropriate boundary conditions that must be applied to the solid. We note that within the contact region, the surface compressive stress is the same as the applied pressure $P(x)$ whilst outside it is identically zero. The correct surface boundary conditions are then

$$\frac{\partial^2 \phi}{\partial x^2}(x,0) = -P(x), \qquad (-L < x < L), \tag{6}$$

$$\frac{\partial^2 \phi}{\partial x \partial y}(x,0) = 0, \qquad (-L < x < L). \tag{7}$$

which represent a frictionless contact, where $P(x)$ is defined as

$$P(x) = \begin{cases} p(x) & |x| \leq a, \\ 0 & |x| > a, \end{cases} \tag{8}$$

so that it is non-zero only in an interval $-a \leq x \leq a$. The radiation condition $|\phi| \to 0$ as $y \to -\infty$ is also imposed to ensure a bounded solution in the region under study.

To fully specify the problem for ϕ, an additional four boundary conditions are required at $x = \pm L$. As the boundaries $x = \pm L$ represent the limits at which the applied pressure is hypothesised to cease to have an effect on the solid, we stipulate that the normal stresses σ_{xx} must vanish there. We therefore have

$$\frac{\partial^2 \phi}{\partial y^2}(-L,y) = \frac{\partial^2 \phi}{\partial y^2}(L,y) = 0. \tag{9}$$

Additionally, we assume that the vertical displacement of the solid vanishes at $x = \pm L$. Therefore, we also impose $v(-L,y) = v(L,y) = 0$. The full problem to solve is now

$$\nabla^4 \phi - 2\alpha \frac{\partial}{\partial y}(\nabla^2 \phi) + \alpha^2 \nabla^2 \phi - \frac{\alpha^2}{1-\nu} \frac{\partial^2 \phi}{\partial x^2} = 0, \qquad -L \leq x \leq L, -\infty < y \leq 0, \tag{10}$$

$$\frac{\partial^2 \phi}{\partial x^2} + P(x) = 0, \qquad y = 0, -L \leq x \leq L, \tag{11}$$

$$\frac{\partial^2 \phi}{\partial x \partial y} = 0, \qquad y = 0, -L \leq x \leq L, \tag{12}$$

$$\frac{\partial^2 \phi}{\partial y^2} = v = 0, \qquad x = -L, -\infty \leq y < 0, \tag{13}$$

$$\frac{\partial^2 \phi}{\partial y^2} = v = 0, \qquad x = L, -\infty \leq y < 0, \tag{14}$$

$$|\phi| \to 0, \qquad y \to -\infty, -L \leq x \leq L. \tag{15}$$

A discussion on the selection of appropriate choices of the interval length L is provided later in section 3.

In order to solve this PDE, we initially transform the horizontal variable so that the solid occupies the region $0 \leq \zeta \leq L, -\infty < y \leq 0$. The required transformation is

$$\zeta = \frac{1}{2}(x+L), \tag{16}$$

which allows us to deduce that

$$\frac{\partial}{\partial x} = \frac{\partial}{\partial \zeta}\frac{\mathrm{d}\zeta}{\mathrm{d}x} = \frac{1}{2}\frac{\partial}{\partial \zeta}. \tag{17}$$

The PDE to be solved now for the stress function ϕ in terms of the new variables is

$$\frac{\partial^4\phi}{\partial\zeta^4} + 8\frac{\partial^4\phi}{\partial\zeta^2\partial y^2} + 16\frac{\partial^4\phi}{\partial y^4} - 8\alpha\frac{\partial}{\partial y}\left(\frac{\partial^2\phi}{\partial\zeta^2} + 4\frac{\partial^2\phi}{\partial y^2}\right) + 4\alpha^2\left(4\frac{\partial^2\phi}{\partial y^2} - \frac{\nu}{1-\nu}\frac{\partial^2\phi}{\partial\zeta^2}\right) = 0 \tag{18}$$

which holds in the region $0 \leq \zeta \leq L, -\infty < y \leq 0$. The boundary conditions under the transformation become

$$\frac{\partial^2\phi}{\partial\zeta^2} + 4P(\zeta) = 0, \qquad y = 0, 0 \leq \zeta \leq L, \tag{19}$$

$$\frac{\partial^2\phi}{\partial\zeta\partial y} = 0, \qquad y = 0, 0 \leq \zeta \leq L, \tag{20}$$

$$\frac{\partial^2\phi}{\partial y^2} = v = 0, \qquad \zeta = 0, -\infty < y \leq 0, \tag{21}$$

$$\frac{\partial^2\phi}{\partial y^2} = v = 0, \qquad \zeta = L, -\infty < y \leq 0, \tag{22}$$

$$|\phi| \to 0, \qquad y \to -\infty, 0 \leq \zeta \leq L,. \tag{23}$$

We now attempt to solve the transformed problem by seeking separable solutions of the form

$$\phi(\zeta, y) = f(y)(A\cos(k\zeta) + B\sin(k\zeta)), \tag{24}$$

for some $k > 0$, which we insist must satisfy the boundary conditions at $\zeta = 0$ and $\zeta = L$. It is found that there are an infinite number of functions of the form

$$\phi_n(\zeta, y) = f_n(y)\sin\left(\frac{n\pi\zeta}{L}\right) \tag{25}$$

$n \in \mathbb{N}$ which satisfy the boundary conditions on ζ. As a result, we formulate the solution to this problem as

$$\phi(\zeta, y) = \sum_{n=1}^{\infty} f_n(y)\sin\left(\frac{n\pi\zeta}{L}\right). \tag{26}$$

In order to determine the functions $f_n(y)$, we substitute (26) into (18). This yields the fourth order ODE

$$\frac{\mathrm{d}^4 f_n}{\mathrm{d}y^4} - 2\alpha\frac{\mathrm{d}^3 f_n}{\mathrm{d}y^3} + \frac{1}{2}(2\alpha^2 - \beta_n^2)\frac{\mathrm{d}^2 f_n}{\mathrm{d}y^2} + \frac{1}{2}\alpha\beta_n^2\frac{\mathrm{d}f_n}{\mathrm{d}y} + \frac{\beta_n^2}{16}\left(\beta_n^2 + \frac{4\alpha^2\nu}{1-\nu}\right) f_n = 0, \tag{27}$$

in which $\beta_n = n\pi/L$ has been used as shorthand notation. We note that all coefficients appearing in this equation are constants. This suggests that we can seek solutions to this equation of the form

$$f_n(y) = C_n e^{\lambda_n y} \tag{28}$$

where C_n are arbitrary constants. Substituting this expression into (27) gives the quartic equation

$$\lambda_n^4 - 2\alpha\lambda_n^3 + \frac{1}{2}(2\alpha^2 - \beta_n^2)\lambda_n^2 + \frac{1}{2}\alpha\beta_n^2\lambda_n + \frac{\beta_n^2}{16}\left(\beta_n^2 + \frac{4\alpha^2\nu}{1-\nu}\right) = 0 \tag{29}$$

which can be solved to give

$$\lambda_n^{(1)} = \left(\frac{1}{4}(\alpha^2+\beta_n^2) + \frac{i}{2}\beta_n\alpha\sqrt{\frac{\nu}{1-\nu}}\right)^{\frac{1}{2}} + \frac{1}{2}\alpha, \tag{30}$$

$$\lambda_n^{(2)} = -\left(\frac{1}{4}(\alpha^2+\beta_n^2) + \frac{i}{2}\beta_n\alpha\sqrt{\frac{\nu}{1-\nu}}\right)^{\frac{1}{2}} + \frac{1}{2}\alpha, \tag{31}$$

$$\lambda_n^{(3)} = \left(\frac{1}{4}(\alpha^2+\beta_n^2) - \frac{i}{2}\beta_n\alpha\sqrt{\frac{\nu}{1-\nu}}\right)^{\frac{1}{2}} + \frac{1}{2}\alpha, \tag{32}$$

$$\lambda_n^{(4)} = -\left(\frac{1}{4}(\alpha^2+\beta_n^2) - \frac{i}{2}\beta_n\alpha\sqrt{\frac{\nu}{1-\nu}}\right)^{\frac{1}{2}} + \frac{1}{2}\alpha.. \tag{33}$$

The general solution of $\phi(\zeta, y)$ is then

$$\phi(\zeta, y) = \sum_{n=1}^{\infty}\left(A_n e^{\lambda_n^{(1)}y} + B_n e^{\lambda_n^{(2)}y} + C_n e^{\lambda_n^{(3)}y} + D_n e^{\lambda_n^{(4)}y}\right)\sin(\beta_n\zeta). \tag{34}$$

In order to satisfy the radiation condition (23), we set $B_n = D_n = 0\ \forall n \in \mathbb{N}$. Applying the remaining boundary conditions on the surface of the solid (19)-(20) gives the particular solution to the transformed problem as

$$\phi(\zeta, y) = 4\sum_{n=1}^{\infty}\frac{P_n e^{\psi_n y}}{\mu_n\beta_n^2}\left(\psi_n\sin(\mu_n y) - \mu_n\cos(\mu_n y)\right)\sin(\beta_n\zeta) \tag{35}$$

where $\psi_n = \mathrm{Re}(\lambda_n^{(1)})$ and $\mu_n = \mathrm{Im}(\lambda_n^{(1)})$, $n \in \mathbb{N}$. The constants P_n, $n \in \mathbb{N}$ are the coefficients in the Fourier series representation of the pressure and are defined as

$$\begin{aligned} P_n &= -\frac{2}{L}\int_{\frac{1}{2}(L-a)}^{\frac{1}{2}(L+a)} p(\zeta)\sin(\beta_n\zeta)\mathrm{d}\zeta, \\ &= -\frac{1}{L}\int_{-a}^{a} p(x)\sin\left(\frac{1}{2}\beta_n(x+L)\right)\mathrm{d}x. \end{aligned} \tag{36}$$

We may now use (35) and (16) to give the solution of the original problem as

$$\phi(x,y) = 4\sum_{n=1}^{\infty} \frac{P_n e^{\psi_n y}}{\mu_n \beta_n^2} \left(\psi_n \sin(\mu_n y) - \mu_n \cos(\mu_n y) \right) \sin\left(\frac{1}{2}\beta_n (x+L) \right). \tag{37}$$

The sub-surface stresses are now readily calculated and are found to be

$$\sigma_{yy} = -\sum_{n=1}^{\infty} \frac{P_n e^{\psi_n y}}{\mu_n} \left(\psi_n \sin(\mu_n y) - \mu_n \cos(\mu_n y) \right) \sin\left(\frac{1}{2}\beta_n (x+L) \right), \tag{38}$$

$$\sigma_{xx} = 4\sum_{n=1}^{\infty} \frac{P_n (\psi_n^2 + \mu_n^2) e^{\psi_n y}}{\mu_n \beta_n^2} \left(\psi_n \sin(\mu_n y) + \mu_n \cos(\mu_n y) \right) \sin\left(\frac{1}{2}\beta_n (x+L) \right), \tag{39}$$

$$\tau_{xy} = -2\sum_{n=1}^{\infty} \frac{P_n (\psi_n^2 + \mu_n^2) e^{\psi_n y}}{\mu_n \beta_n} \sin(\mu_n y) \cos\left(\frac{1}{2}\beta_n (x+L) \right). \tag{40}$$

The vertical deflection may also be calculated by integrating (5) over the interval $(-\infty, y)$ which yields

$$\begin{aligned} v(x,y) = -\frac{(1+\nu)}{E_0} \sum_{n=1}^{\infty} \frac{P_n}{\mu_n} \Bigg[& (1-\nu) \left(\psi_n I_1^{(n)}(y) - \mu_n I_2^{(n)}(y) \right) \\ & + \frac{4\nu(\psi_n^2 + \mu_n^2)}{\beta_n^2} \left(\psi_n I_1^{(n)}(y) + \mu_n I_2^{(n)}(y) \right) \Bigg] \sin\left(\frac{1}{2}\beta_n (x+L) \right). \end{aligned} \tag{41}$$

where

$$I_1^{(n)}(y) = \frac{e^{(\psi_n - \alpha)y}}{\mu_n^2 + (\psi_n - \alpha)^2} \left(\mu_n \sin(\mu_n y) + (\psi_n - \alpha) \cos(\mu_n y) \right), \tag{42}$$

$$I_2^{(n)}(y) = \frac{e^{(\psi_n - \alpha)y}}{\mu_n^2 + (\psi_n - \alpha)^2} \left((\psi_n - \alpha) \sin(\mu_n y) - \mu_n \cos(\mu_n y) \right). \tag{43}$$

2.1. Maximum penetration depth

The radiation boundary condition (23) ensures that each harmonic component (Fourier mode) vanishes at infinity. However, in practice, the influence of a harmonic component is lost when the predicted contribution is smaller than computer error. Teodorescu *et al.* [19] showed that in a semi-infinite solid split into two distinct yet homogeneous layers, the depth at which the contribution of each individual harmonic becomes negligible is inversely proportional to the harmonic order. We may perform a similar investigation here by monitoring the exponential term $e^{\psi_n y}$ which is responsible for the decay of the stress components (38), (39), (40) and the vertical displacement (41). We set a minimum value ($\kappa = 10^{-10}$) and assume that when $e^{\psi_n y} \leq \kappa$, the contribution of that harmonic component is negligible. Therefore, the maximum penetration depth is $y_{lim} = \ln \kappa / \psi_n$.

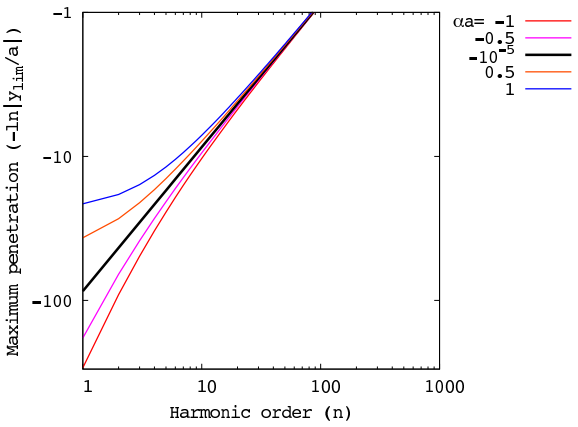

(a)

Figure 2: An investigation into the maximum penetration depth for each harmonic order for five different materials.

Figure 2) shows the maximum penetration depth for the first 100 harmonic components appearing in the solutions of the stresses and vertical displacement. It is seen that higher harmonic orders have a shallower penetration than lower harmonic orders. This means that away from the surface of the solid, the higher frequency wave modes do not affect the solutions of the stresses and displacement and hence a partial sum of only the first few fourier modes will be sufficient to accurately describe the behaviour of the stresses far beneath the solid surface. We additionally note as $\hat{\alpha}$ becomes increasingly positive, each harmonic component penetrates less into the depth of the solid. This is indicative that materials which become increasingly soft below the surface experience stresses which die away much faster in the limit $y \to -\infty$.

Figures 3a) and 3b) show the decay of $e^{\Psi_n y}$ for two representative harmonics ($n = 1$ and $n = 100$) subject to different values of $\hat{\alpha}$. These results reiterate the previous findings and clearly shows how softening media dampens the contribution of lower harmonics.

It should be noted that the wavelength of the lowest harmonic captured by this solution depends on the choice of decomposition interval $[-L, L]$. As the contact is assumed to be smooth, we do not account for any waviness of the solid surface. If this model were to be adapted to a rough contact, the size of the interval should be carefully chosen to ensure that any waviness of the the solid itself is accurately captured. This requires the wavelength of the lowest harmonic component to be greater than the largest wavelength of the solid surface. However, this comes at a high computational cost as our model would need to encompass more Fourier modes to accurately capture the solution.

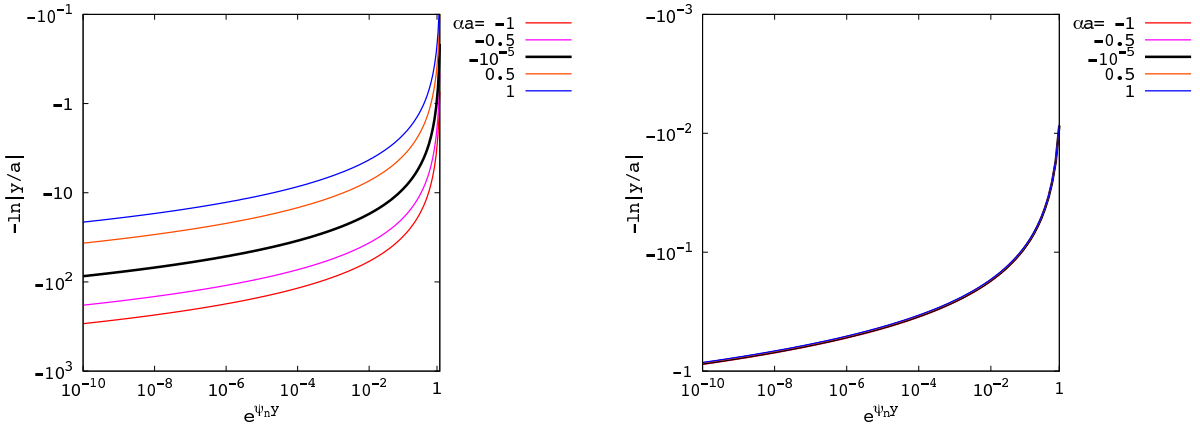

(a) (b)

Figure 3: An investigation into the decay of $e^{\psi_n y}$ for five different materials. The pictures show a) the decay rate of the first harmonic order $(n = 1)$ and b) the decay rate of the hundredth harmonic order $(n = 100)$.

3. Results

To highlight some of the most significant advantages of the current model we consider producing results for a simple pressure function. Please note that in practical applications the infinite summations in equations (38), (39), (40) and (41) are limited by computer capabilities and hence we must truncate the summations appearing in these equations at some finite value N. Thus, we now take the solutions for the stresses and vertical displacement as

$$\sigma_{yy} = -\sum_{n=1}^{N} \frac{P_n e^{\psi_n y}}{\mu_n} \left(\psi_n \sin(\mu_n y) - \mu_n \cos(\mu_n y) \right) \sin\left(\frac{1}{2}\beta_n (x+L) \right), \tag{44a}$$

$$\sigma_{xx} = 4\sum_{n=1}^{N} \frac{P_n (\psi_n^2 + \mu_n^2) e^{\psi_n y}}{\mu_n \beta_n^2} \left(\psi_n \sin(\mu_n y) + \mu_n \cos(\mu_n y) \right) \sin\left(\frac{1}{2}\beta_n (x+L) \right), \tag{44b}$$

$$\tau_{xy} = -2\sum_{n=1}^{N} \frac{P_n (\psi_n^2 + \mu_n^2) e^{\psi_n y}}{\mu_n \beta_n} \sin(\mu_n y) \cos\left(\frac{1}{2}\beta_n (x+L) \right), \tag{44c}$$

$$\begin{aligned} v(x,y) = -\frac{(1+\nu)}{E_0} \sum_{n=1}^{N} \frac{P_n}{\mu_n} \Bigg[(1-\nu) \left(\psi_n I_1^{(n)} - \mu_n I_2^{(n)} \right) \\ + \frac{4\nu(\psi_n^2 + \mu_n^2)}{\beta_n^2} \left(\psi_n I_1^{(n)} + \mu_n I_2^{(n)} \right) \Bigg] \sin\left(\frac{1}{2}\beta_n (x+L) \right). \end{aligned} \tag{44d}$$

3.1. Example 1: Symmetric pressure profile

We consider the pressure function

$$p(x) = p_0 \cos\left(\frac{\pi x}{2a} \right) \tag{45}$$

which is symmetric about the origin (see figure 4). As the pressure given here is analytic, we can readily calculate the coefficients P_n and find that

$$P_{2m-1} = \frac{4(-1)^m aL}{\pi(a^2(2m-1)^2 - L^2)} \cos\left(\frac{(2m-1)\pi a}{2L}\right), \tag{46}$$

$$P_{2m} = 0, \tag{47}$$

for $m \geq 1$, so that the stresses and displacements inherent in this problem consist of only odd numbered Fourier modes.

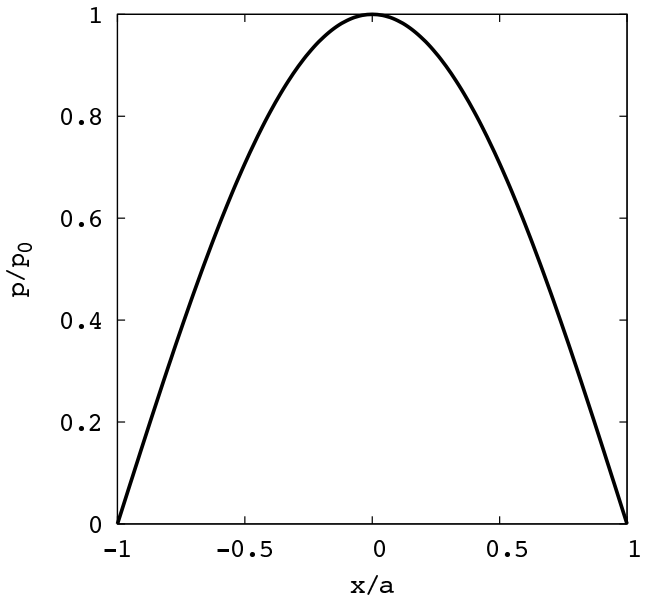

Figure 4: The pressure function applied in example 1 over the dimensionless contact region $[-1,1]$.

Before we consider presenting numerical results for this problem, we must determine an appropriate value of L. In order to do this, we consider plots of the maximum value of the dimensionless surface deflection $(\hat{v}_{\max})$ and the maximum value of the dimensionless principal stress $(\hat{\tau}_{\max})$ against the non-dimensional variable L/a. We hope that these graphs will show that for sufficiently large values of L, both the maximum surface deflection and principal stress will converge which indicates that taking increasingly large interval lengths means that we are not gaining any additional information. Note that for convenience, the notation

$$\hat{v}_{\max} = \frac{1}{a}\max\big(v(0,0)\big),$$

$$\hat{\tau}_{\max} = \frac{1}{p_0}\max\left(\tau_1\right)$$

has been adopted.

Figure (5) depicts the values of $\hat{v}_{\max}$ and $\hat{\tau}_{\max}$ obtained for six different values of $\hat{\alpha}$ subject to the applied pressure given by (45).

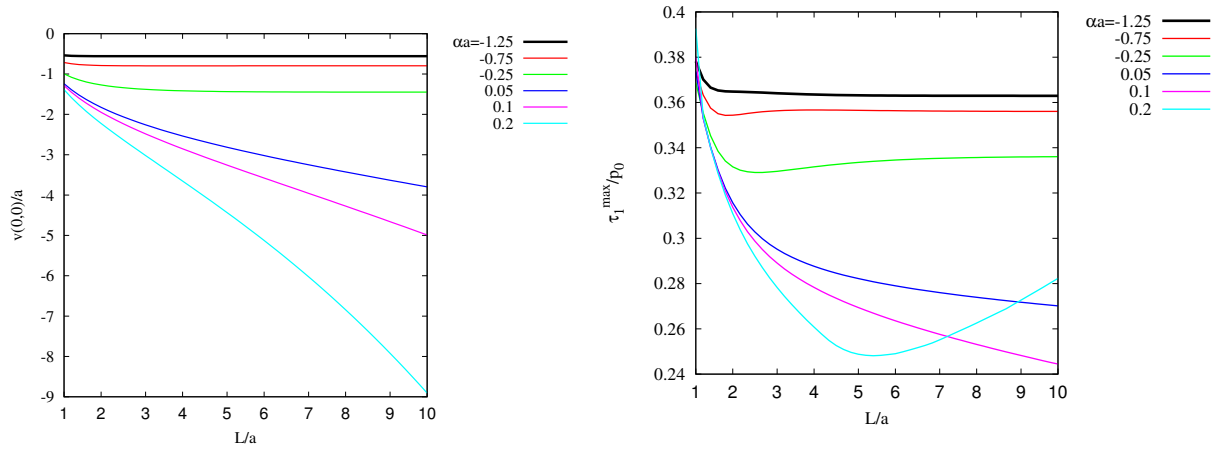

(a) (b)

Figure 5: Plots of L/a vs a) $\hat{v}_{\max}$ and b) $\hat{\tau}_{\max}$ for six different values of $\hat{\alpha}$ corresponding to both hardening and softening media.

It is easily observed from these results that the maximum surface deflection and maximum principal stress corresponding to materials that become increasingly hard below the surface ($\hat{\alpha} < 0$) exhibit convergence as L/a increases. Conversely, if $\hat{\alpha} > 0$, the maximum surface deflection and maximum principal stress exhibit no convergence which indicates that this solution method fails for materials that become increasingly soft below the surface. This observation is not surprising given the unrealistic physical situation of a material becoming infinitely soft (E$\rightarrow$ 0) far below its surface which is what $\hat{\alpha} > 0$ represents.

It should also be noted from figure 5b), that as the results presented are dimensionless, the choice of the parameter L is insensitive to the load. This seems to indicate that only the growth rate of the modulus of elasticity is important in determining the interval of decomposition.

Utilising the information in figure 5, we choose $L/a = 6$, $\nu = 0.25$, $N = 200$ to produce results for this example and restrict our attention to materials that exhibit sub-surface stiffening ($\hat{\alpha} < 0$). We note that if $\alpha = 0$, equation (29) does not provide four linearly independent roots and the analytic approach given above is no longer valid. However, it should be noted that $\alpha = 0$ corresponds to a homogeneously elastic solid. Therefore, the subsurface stress field and vertical deflection can be predicted by alternate methods (e.g. Teodorescu *et al* [19]). In the current study we use as a control case a semi-infinite solid with a very small growth rate ($\hat{\alpha} = -10^{-5}$). We compare the results with materials with increasing stiffness.

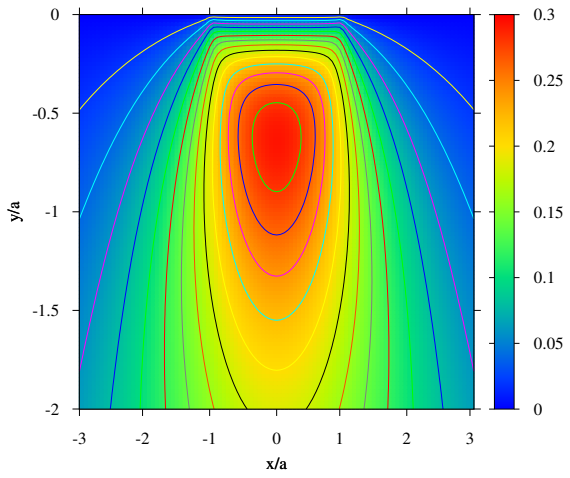

Figure 6: Contour plots of the non-dimensional principal shear stresses τ_1/p_0 for a semi-infinite solid with $\hat{\alpha} = -10^{-5}$

Figure 6 shows the contour plot of the non-dimensional principal stress τ_1/p_0 for the control case and figure 7 shows similar plots for several materials with increasing subsurface stiffness ($\hat{\alpha} < 0$). For clarity, only the stresses in the immediate vicinity of the contact region are presented ($-3 \leq x/a \leq 3, -2 \leq y/a \leq 0$).

It is immediately seen here that as $\hat{\alpha}$ becomes increasingly negative (material stiffening), the maximum principal stress increases in magnitude. Additionally, we see that the region in which the maximum stresses occur moves closer to the solid surface and becomes thinner as the solid becomes increasingly stiff. This indicates that materials with increasing sub-surface stiffness are more resistant to the applied pressure than softer materials and will thus experience less vertical displacement than more pliable materials. We may compare the exponential increase in stiffness here to that of a thick protective coating. A possible example is that of a journal bearing shell which requires a soft protective layer on the lubricated side. This encourages local deformation, increases the lubricant film thickness and reduces friction. However, at the same time a harder base is necessary to provide the overall stiffness of the shell. The rate with which the local stiffness morphs from one material to the other determines the efficiency of the bearing.

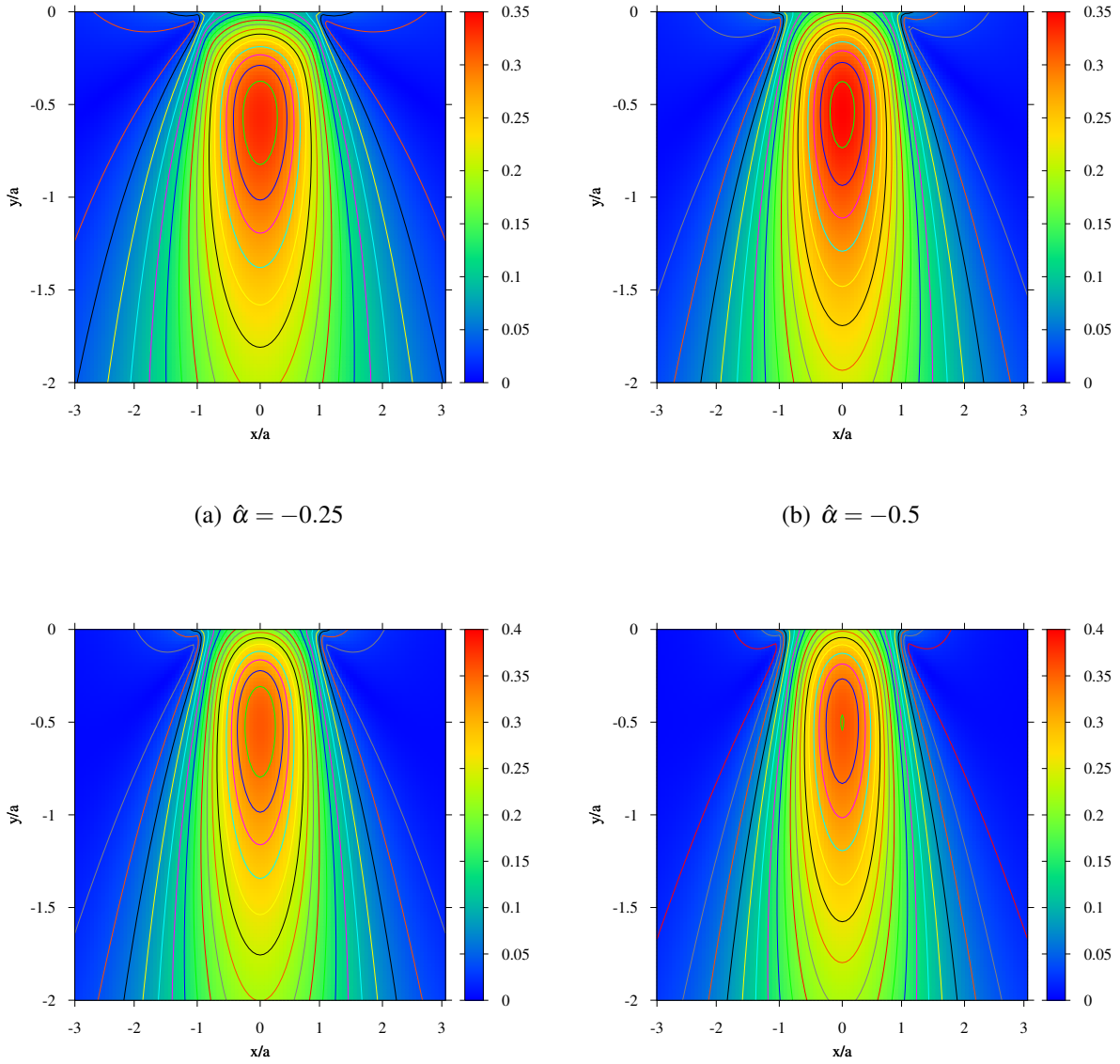

(a) $\hat{\alpha} = -0.25$

(b) $\hat{\alpha} = -0.5$

(c) $\hat{\alpha} = -0.75$

(d) $\hat{\alpha} = -1$

Figure 7: The influence of elastic gradient on the non-dimensional principal stress field (τ_1/p_0) for four differents materials with increasing stiffness.

An alternate way of viewing the behaviour of the sub-surface stresses present in the solid is to take a cut through the x-axis and investigate how the principal stresses change below a fixed point on the surface. Figure (8) depicts the principal stresses within the solid beneath the origin $(x = 0)$ and the edge of the contact region $(x = a)$. It is seen in figure (8a) that the stresses corresponding to

solids that become increasingly stiff below their surface are larger in magnitude everywhere than those present within softer materials. This trend can additionally be seen in figure (7).

The results presented in figure (8b) are more interesting. We see here that on the solid surface the stresses present within the harder solids are larger than those in the softer materials. This is also the case far below the solid surface. However, we see that between $-2 \leq y/a \leq -0.1$, the stresses within the softer materials become larger than those in the harder material. They suggest that the stresses induced within solids that become increasingly stiff below their surface penetrate further into the solid yet decay more quickly outside of the contact area. This behaviour is not immediately obvious in figure (7) but is readily seen here.

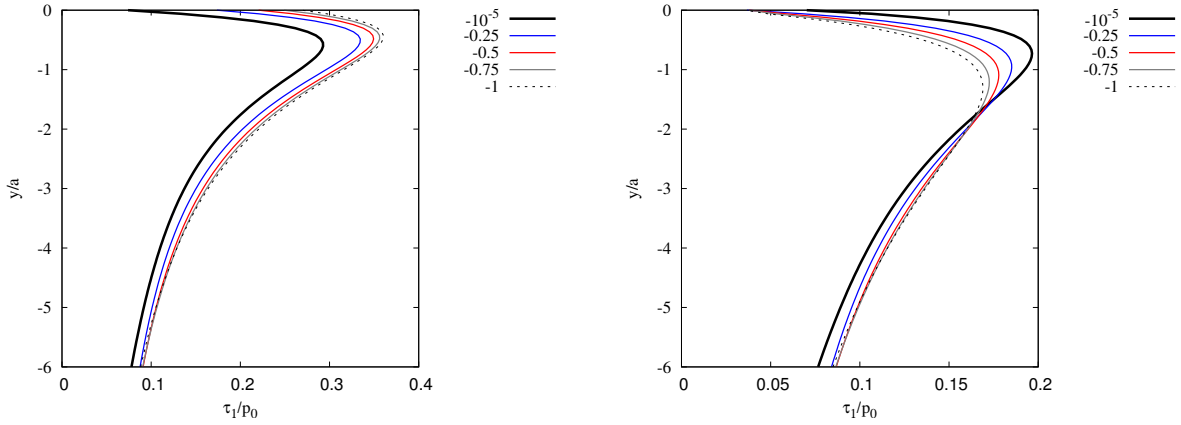

(a) $x/a = 0$ (b) $x/a = 1$

Figure 8: Non-dimensional principal stresses τ_1/p_0 at $x/a = 0$ and $x/a = 1$ for several values of $\hat{\alpha} = 0$.

Figure 9 shows the influence of the elastic gradient on the dimensionless surface deflection for the values of α given in figures (6) and (7). It is seen here that the surface deflection decreases as $\hat{\alpha}$ becomes increasingly more negative. These results are intuitively correct and are in accord with literature accepted results [19].

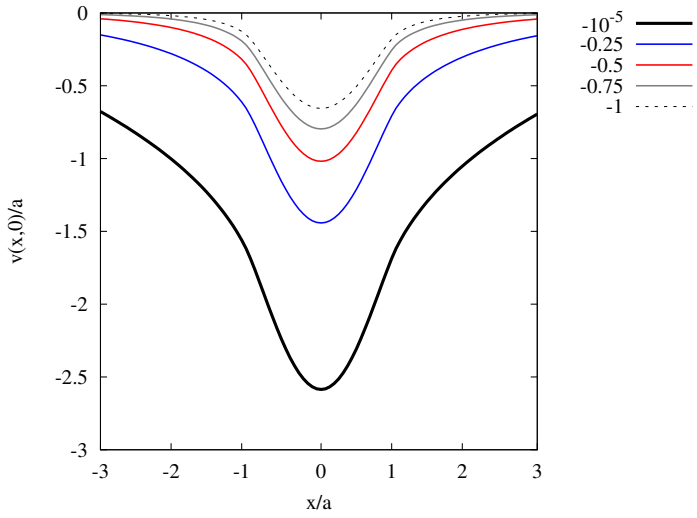

Figure 9: Normalised surface deflections (example 1)

4. Contact by a rigid punch

So far in this paper, we have considered producing results when both the applied pressure and contact half-width are known. In many contact problems, both of these quantities will be unknown and need to be determined as part of the solution procedure. In this section, we present an algorithm which may be used to determine the pressure which results from the contact of a rigid punch. We firstly discuss how approximations to the contact pressure may be derived and then present a solution technique which allows accurate estimation of the contact half-width.

4.1. Approximations to the contact pressure

We initially see from (41) that the vertical displacement of the solid surface may be written as

$$v(x,0) = \hat{v}(x) = \sum_{n=1}^{\infty} \mathscr{J}_n P_n \phi_n(x) \tag{48}$$

where

$$\mathscr{J}_n = \frac{-(1+\nu)P_n}{E_0\beta_n^2(\mu_n^2+(\psi_n-\alpha)^2)}\left((1-\nu)(\alpha-2\psi_n)\beta_n^2 - 4\nu\alpha(\psi_n^2+\mu_n^2)\right) \tag{49}$$

and

$$\phi_n(x) = \sin\left(\frac{1}{2}\beta_n(x+L)\right) \tag{50}$$

for $n \in \mathbb{N}$. Taking the derivative of (48) with respect to x gives the gradient of deflection on the solid surface as

$$\hat{v}^{'}(x) = \sum_{n=1}^{\infty} \mathscr{J}_n P_n \phi_n^{'}(x), \qquad (-L \leq x \leq L). \tag{51}$$

If we consider indenting the surface of the solid by a rigid punch, we will know the deflection gradient on the surface because the shape of the punch will be known. This means that the function $\hat{v}^{'}$ will be known and thus the only unknowns within (51) are the coefficients in the Fourier representation of the pressure. If we replace all coefficients P_n appearing in (51) using (36) we obtain

$$\hat{v}^{'}(x) = -\frac{1}{L} \int_{-a}^{a} \sum_{n=1}^{\infty} \mathscr{J}_n \phi_n^{'}(x) \phi_n(t) p(t) \mathrm{d}t \tag{52}$$

which is a Fredholm integral equation of the first kind. This may also be written in operator form as

$$\hat{v}^{'}(x) = -\frac{1}{L} (\mathscr{L} p)(x). \tag{53}$$

As this equation is non-singular, we can approximate the contact pressure using Galerkin's method. This involves consideration of the weak form of (52) which is attained by multiplying by the test functions $\chi_j(x)$, $j = 1, ..., M$ and integrating over the contact region. The resultant equations are then

$$(\hat{v}, \chi_j) = -\frac{1}{L} (\mathscr{L} p, \chi_j), \tag{54}$$

$j = 1, ..., M$, where the notation

$$(f, g) = \int_{-a}^{a} f(x) g(x) \mathrm{d}x \tag{55}$$

has been used to simplify this expression. Introducing the approximation

$$p(x) = \sum_{i=1}^{M} \gamma_i \chi_i(x) \tag{56}$$

allows us to reduce (54) to the system

$$V = -\frac{1}{L} \Delta^T \gamma, \tag{57}$$

where

$$V = \Big((\hat{v}, \chi_1), (\hat{v}, \chi_2), ..., (\hat{v}, \chi_M) \Big)^T, \tag{58}$$

and the entries of matrix Δ are defined as $(\Delta)_{ij} = (\mathscr{L}\chi_i, \chi_j)$. Equation (57) can be rearranged to give

$$\gamma = -L\Delta^{-T}V \tag{59}$$

which furnishes us with an analytic approximation to the contact pressure via (56). This approximation can then be used to compute the Fourier coefficients P_n which in turn allows the determination of the sub-surface stresses and vertical deflection via (44a)-(44d) as before.

It should be noted that this method can be used to solve for the contact pressure induced by a punch of arbitrary shape as long as V is not identically zero.

4.2. Approximating the contact half width

In many contact problems, the total applied load (W) is given rather than the contact half-width. It is known that increased loads give rise to larger contact regions and thus we may deduce that each value of W gives rise to a unique contact half-width subject to fixed material parameters (ν, E_0, α). This enables us to solve for the contact half width using iterative techniques.

The total load and contact pressure are related via

$$W = \int_{-a}^{a} p(x)\mathrm{d}x \approx \sum_{n=1}^{\infty} \gamma_i \int_{-a}^{a} \chi_i(x)\mathrm{d}x \tag{60}$$

which follows from (56). We now define

$$f(a) = W - \sum_{n=1}^{\infty} \gamma_i \int_{-a}^{a} \chi_i(x)\mathrm{d}x \tag{61}$$

which will be vanishingly small provided that the approximation derived above is sufficiently accurate. This equation may be solved iteratively for a using the secant method

$$a_{n+1} = a_n - \frac{\delta f(a_n)}{f(a_n+\delta) - f(a_n)} \tag{62}$$

where $\delta > 0$ is some constant. The total solution procedure is then to determine the contact pressure (56) for each value of a_n, determine $f(a_n)$ and $f(a_n+\delta)$ and update the approximation to a using (62) until the desired accuracy has been reached. In this paper, we determine whether or not we have converged to the contact half-width using the criterion

$$\frac{|a_{n+1} - a_n|}{|a_{n+1}|} < \varepsilon \tag{63}$$

which provides a measure of the residual error between the current and previous guesses. Within this work we choose $\varepsilon = \delta = 1 \times 10^{-7}$. Figure (10) gives a flowchart of the steps to be followed in this solution method.

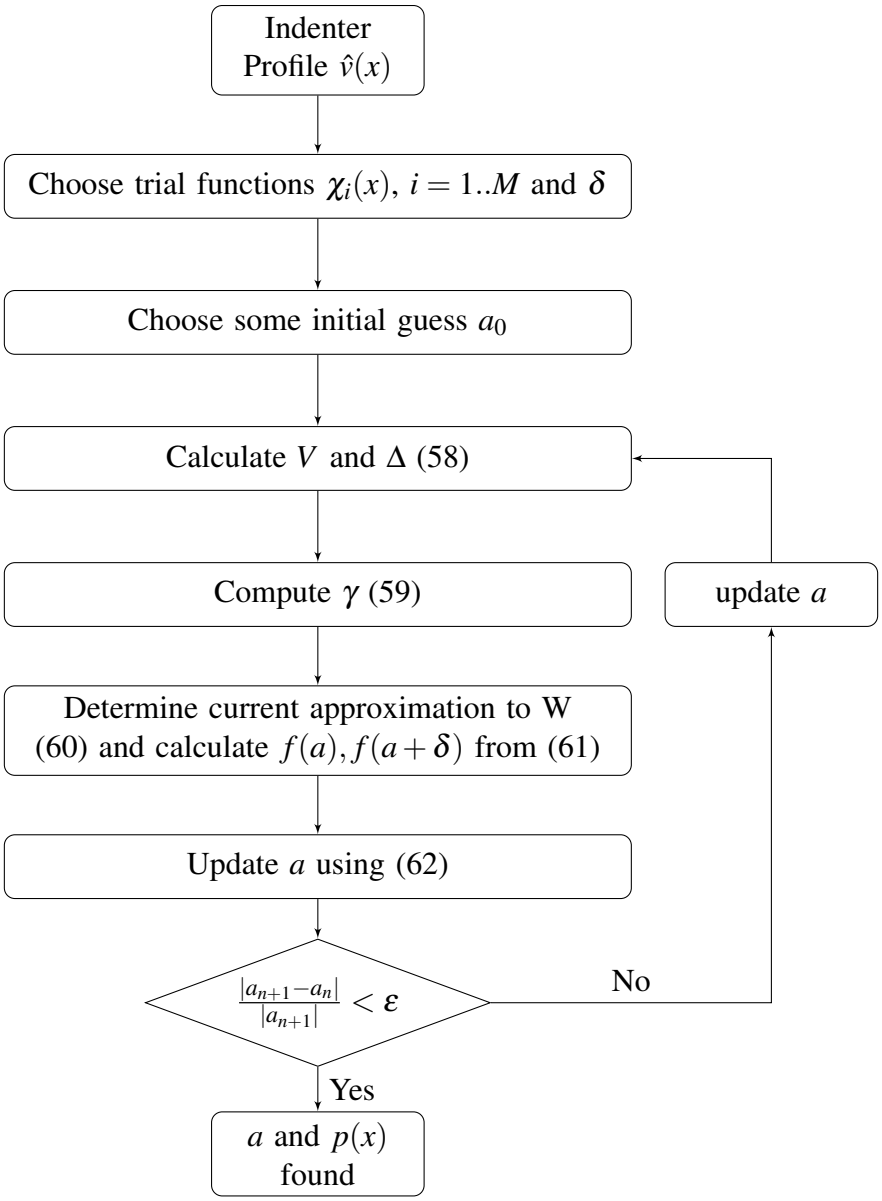

Figure 10: Flow chart of the iterative algorithm derived in this section

4.3. Example: Cylindrical punch

We examine the accuracy of the proposed approximations above by considering contact by a rigid cylindrical punch. Modelling the stamp profile as a quadratic in the vicinity of the contact gives

$$\hat{v}(x) = -\varepsilon_0 + \frac{x^2}{2R} \tag{64}$$

where R is the radius of the punch and ε_0 is the as yet unknown maximum deflection of the solid surface. The punch is taken to have radius 10cm and length 20cm and the load resulting from the

contact is 200N. The other parameters considered are $\nu = 0.42$ and $E_0 = 69$GPa. This physical situation may be viewed as a space bearing coated by a thick gold layer.

As Hertzian theory provides an analytical solution for this problem when the solid is homogeneously elastic, we choose $a_0 = a_h$ where a_h is the contact half width predicted by Hertz. This value is calculated as

$$a_h = \sqrt{\frac{4(1-\nu^2)WR}{\pi E_0}} \tag{65}$$

which in this case gives $a_h = 17.434\mu m$. We can also compute the predicted maximum Hertzian pressure which is given by the formula

$$P_h = \frac{2W}{\pi a_h}. \tag{66}$$

In this particular example $P_h = 7.303 \times 10^6$Pa. It will be of primary interest in this example to determine how sub-surface stiffening affects the predicted pressures and contact half widths and how accurate Hertzian theory is under such conditions. As a is unknown in this problem prior to solving for the contact pressure, we cannot fix the parameter $\hat{\alpha}$ within this example. We can however fix the parameter $\alpha a_h = -1 \times 10^{-4}, -0.5 - 1, -2$ which represent different degrees of sub-surface stiffening. The first value $\alpha a_h = -1 \times 10^{-4}$ is a control case and should predict a pressure and contact half width that agrees almost exactly with the results of Hertz.

It is only left to choose $\chi_j(x)$, $j = 1, ..., M$ for this example. As it is known that the pressure resulting from contact by a rigid cylindrical punch is identically zero at $x = \pm a$, we choose to represent the contact pressure using simple linear splines. In order to do this, we split the contact region into $M-1$ sub-intervals of width h and thus define

$$\chi_j(x) = \begin{cases} \frac{x - x_{j-1}}{x_j - x_{j-1}}, & x_{j-1} \le x \le x_j, \\ \frac{x_{j+1} - x}{x_{j+1} - x_j}, & x_j \le x \le x_{j+1}, \\ 0, & \text{otherwise} \end{cases} \tag{67}$$

for $j = 2, ..., M-1$. The functions $\chi_1(x)$ and $\chi_M(x)$ are omitted from (56) as $\gamma_1 = \gamma_M = 0$ from the condition that $p(\pm a) = 0$. In this particular example, we take $M = 52$ so that the contact pressure comprises 50 splines.

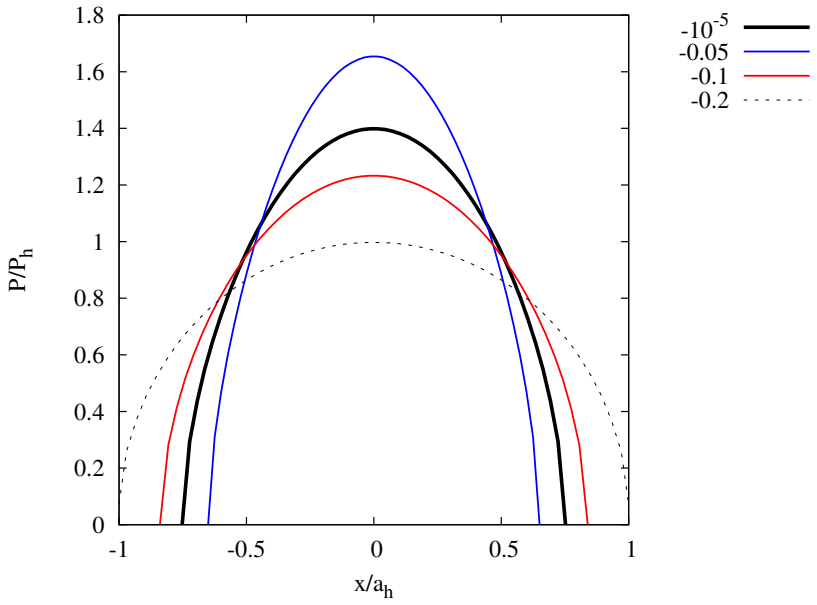

Figure 11: Pressure curves produced using the iterative algorithm given in (61) for αa_h=-1×10^{-4} (blue line), -0.5 (red line), -1 (green line), -2 (black line)

The results produced for this problem are presented in figure (11) and show that as the solid becomes increasingly hard beneath its surface, the maximum contact pressure induced by the cylindrical punch becomes much larger in magnitude whilst the contact region decreases in size. This can be explained by the solid retaining very high stresses immediately beneath its surface over an increasingly small region (a trend originally seen in figure (7)). The control case $\alpha a_h = -1\times10^{-4}$ corresponds to the results given by Hertz exactly as expected and thus validates the predicted results of our model. Figure (12) illustrates the produced sub-surface stress field for the cases $\alpha a_h = -1\times10^{-4}, -0.5-1, -2$. We see here that the maximum principal stress becomes increasingly large as the solid becomes increasingly hard below the surface whilst the region in which the largest principal stresses occur becomes thinner. These results are intuitively correct given the applied surface pressure. It should also be noted that the plot produced in figure (12a) corresponds exactly to the sub-surface stress field resultant from the application of Hertzian pressure to a homogeneously elastic solid.

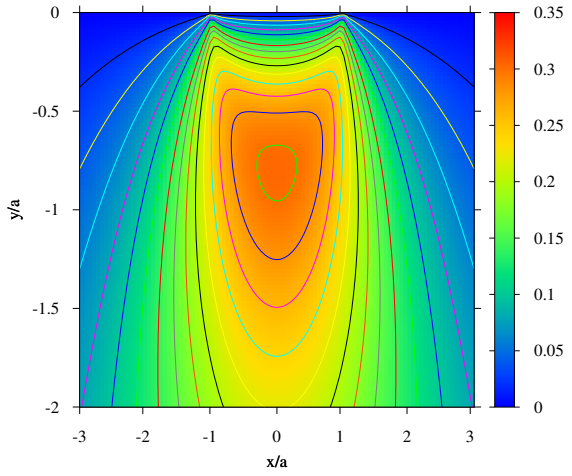

(a) $\alpha a_h = -0.0001$

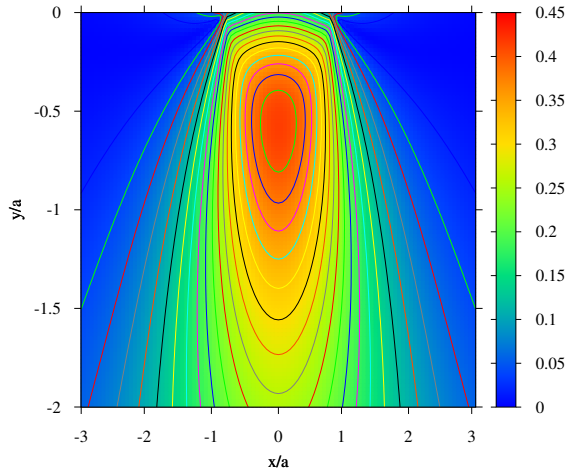

(b) $\alpha a_h = -0.5$

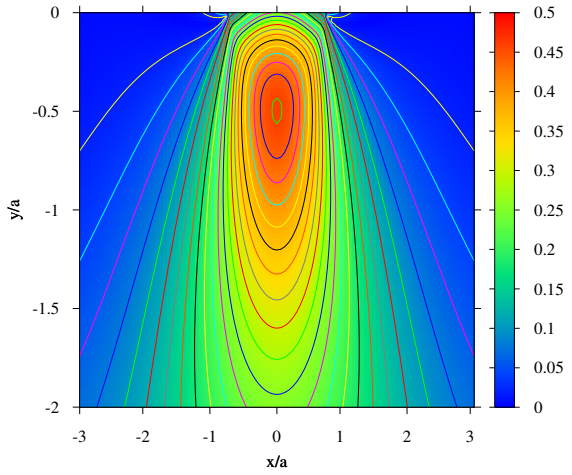

(c) $\alpha a_h = -1$

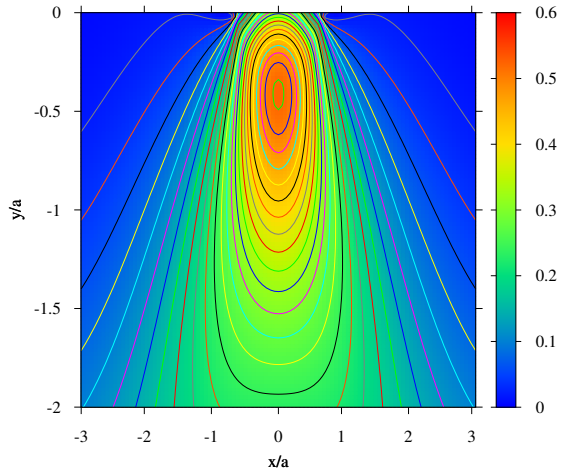

(d) $\alpha a_h = -2$

Figure 12: Plots of the non-dimensional principal stresses produced subject to the contact pressures produced within figure (11) for the values of αa_h given.

Iteration number	Quantity	$\alpha a_h = -1 \times 10^{-4}$	$\alpha a_h = -0.5$	$\alpha a_h = -1$	$\alpha a_h = -2$
1	a_1	17.627227μm	15.002714μm	14.024444μm	13.213606μm
	RE (%)	1.09	16.208	24.313	31.942
2	a_2	17.628885μm	14.653060μm	13.189098μm	11.620017μm
	RE (%)	0.009	2.386	6.334	13.714
3	a_3	17.628908μm	14.638976μm	13.121974μm	11.354339μm
	RE (%)	1.31×10^{-4}	0.0962	0.512	2.334
4	a_4	17.628908μm	14.638636μm	13.119740μm	11.338914μm
	RE (%)	1.83×10^{-6}	0.00232	0.017	0.136
5	a_5	–	14.638628μm	13.119674μm	11.338318μm
	RE (%)	–	5.47×10^{-5}	5.01×10^{-4}	0.005
6	a_6	–	14.638628μm	13.119672μm	11.338296μm
	RE (%)	–	1.2856×10^{-6}	1.466×10^{-5}	1.968×10^{-4}
7	a_7	–	–	13.119672μm	$11.338295\mu m$
	RE (%)	–	–	4.29×10^{-7}	7.367×10^{-6}

Table 1: Updated guesses to the contact half width produced using (62), the number of iterations required to attain a to machine accuracy and the residual error between the current iteration and the previous one.

We have already verified that the results computed using this algorithm are accurate by comparing with classical Hertzian results. However, this method is also computationally cheap to apply as typically only a handful of iterations are needed to compute the contact pressure and contact half width to machine accuracy. Furthermore each iteration takes approximately a quarter of a second to compute. Table (1) details the approximations obtained from (62) to a after each iteration and the residual error between the current and previous guess expressed as a percentage. We note that at most 7 iterations are required to produce the results appearing in figures (11) and (12) whilst only 4 are required for the almost homogeneous solid. This method is therefore extremely fast and computationally efficient to use.

5. Conclusions

We have derived a solution for the stress function which can be used to describe the behaviour of a semi-infinite functionally graded material under pressure. The original problem is mapped into an alternate domain and it is found that the stress function can be represented as a half-range Fourier sine series in these new coordinates. The final solution is then easily computed by rewriting the solution in terms of the original horizontal variable and analytic expressions were presented for the stresses within the solid and the deflection of the solid due to an applied pressure. A simple example pressure was then considered to produce results for this problem and it was found that solids that stiffen beneath their surface experience larger maximum principal stresses in comparison to homogeneous materials.

This paper concluded with the derivation of an efficient iterative algorithm from which the applied pressure and contact half-width a may be determined when a functionally graded solid is contacted by a rigid punch. The accuracy of this method was investigated by considering contact by a rigid circular punch and it was found that the pressure curve and contact half-width produced for a material that is almost homogeneous agrees well the predictions of Hertzian theory. It was further observed that materials that exhibit increased sub-surface stiffness deviate from the predictions of Hertzian theory as the predicted maximum pressure is larger than that of Hertz whilst the contact half-width is smaller.

In summary, the method proposed in this paper is accurate and computationally cheap to apply and could provide a useful tool to the practising engineer.

Acknowledgement

The authors acknowledge the technical support from partners and sponsorship provided by the EPSRC through the ENCYCLOPAEDIC program grant.

References

[1] J. Boussinesq, Application des potentiels *à* l'*é*tude de l'*é*quilibre et du mouvement des solides *é*lastiques, Paris, France, Gauthier-Villars (1885)

[2] A. Flamant, Sur la r*é*partition des pressions dans un solide rectangulaire charg*é* transversalement, Compte. Rendu. Acad. Sci. Paris, 114, 1465 (1892)

[3] M. Hannah, Contact stress determination in a thin elastic layer, Q. J. Mech. Appl. Math. 4l, 94–105 (1951)

[4] R. H. Bentall and K. L. Johnson, Slip in the rolling contact of two dissimilar elastic rollers, International Journal of Mechanical Sciences, 9, 6, 389–404 (1967)

[5] K. L. Johnson, Contact Mechanics, Cambridge University Press, Cambridge (1985)

[6] T. C. OSullivan, R. B. King, Sliding contact stress field due to a spherical indenter on a layered elastic half-space, Trans. ASME J. Trib. 110, 235–240 (1988)

[7] M. J. Jaffar, Asymptotic behaviour of thin elastic layers bonded and unbonded to a rigid foundation, Int. J. Mech. Sci. 31, 229–235 (1989)

[8] J. R. Barber, Contact problems for the thin elastic layer, Int. J. Mech. Sci. 32, 129–132 (1990)

[9] R. E. Gibson, Some Results Concerning Displacements and Stresses in a Non-Homogeneous Elastic Half-space, G*é*otechnique, 17, 1, 58–67 (1967)

[10] J. R. Booker, N. P. Balaam and E. H. Davis, The behaviour of an elastic non-homogeneous half-space. Part II-circular and strip footings, 9 , 4, 369–381, (2005)

[11] S. Suresh, M. Olsson, A. E. Giannakopoulos, N. P. Padture and J. Jitcharoen, Engineering the Resistance to Sliding-Contact Damage Through Controlled Gradients in Elastic Properties at Contact Surfaces, Acta mater. 47, 14, 3915–3926 (1999)

[12] S. Suresh, A. E. Giannakopoulos, N. P. Padture and J. Jitcharoen, Functionally-Graded Materials, European Patent Speciffication, International application number PCT/US98/05188 (1998)

[13] M. A. Guler and F.Erdogan, Contact mechanics of graded coatings, Int. J. Solids Structures, 41, 3865–3889 (2004)

[14] L. L. Ke and Y. S. Wang, Two-dimensional sliding frictional contact of functionally graded materials, European Journal of Mechanics A/Solids 26, 171–188 (2007)

[15] I.N. Sneddon, Fourier Transforms, McGraw-Hill Book Company, New York, (1951)

[16] I.A. Polansky, L.M. Keer, A fast and accurate method for numerical analysis of elastic layered contacts, Trans. ASME J. Tribol., 122 30–35, (2000)

[17] S. Liu, Q. Wang, Studying contact stress fields caused by surface tractions with a discrete convolution and fast fourier transform algorithm, Trans. ASME, J. Tribol., 124, 36–45 (2002)

[18] H.J. Tripp, J. van Kuilenburg, G.E. Morales-Espejel, P. Lugt, Frequency response functions and rough surface stress analysis, Tribology Trans. 46, 376–382 (2003)

[19] M. Teodorescu, H. Rahnejat, R. Gohar and D. Dowson, Harmonic decomposition analysis of contact mechanics of bonded layered elastic solids, Applied Mathematical Modelling, 33, 467–485 (2009)

[20] Y. Xu and D. Zhou, Three-dimensional elasticity solution of functionally graded rectangular plates with variable thickness, Composite Structures, 91, 56–65 (2009)

[21] M. H. Sadd, Elasticity: Theory Applications and Numerics, Elsevier academic press, second edition (2009)

[22] A. E. Giannakopoulos and S. Suresh, Indentation of solids with gradients in elastic properties: Part 1. Point force, Int. J. Solids Structures, 34, 2357–2392 (1997)

[23] S. Chidlow, M. Teodorescu and N.D. Vaughan, A New Solution Method for the Contact Mechanics of Graded Coatings, STLE/ASME International Joint Tribology Conference, San Francisco, California (2010)